



Technical note: Evaluating a geographical information system (GIS)-based approach for determining topographic shielding factors in cosmic-ray exposure dating

Felix Martin Hofmann

5 Institute of Earth and Environmental Sciences, University of Freiburg, Freiburg, 79104, Germany

Correspondence: felix.martin.hofmann@geologie.uni-freiburg.de

Abstract. Cosmic-ray exposure (CRE) dating of boulders on terminal moraines has become a well-established technique to reconstruct glacier chronologies. If topographical obstructions are present in the surroundings of sampling sites, CRE ages need to be corrected for topographic shielding. In recent years, geographical information system (GIS)-based approaches have been developed to compute shielding factors with elevation data, particularly two toolboxes for the ESRI ArcGIS software. So far, the output of the most recent toolbox (Li, 2018) has only been validated with a limited number of field data-based shielding factors. Additionally, it has not been systematically evaluated how the spatial resolution of the input-elevation data affects the output of the toolbox and whether a correction for vegetation leads to considerably more precise shielding factors. This paper addresses these issues by assessing the output of the toolbox with an extensive set of field data-based shielding factors. Commonly used elevation data with different spatial resolutions were tested as input. To assess the impact of the different methods on CRE ages, ages of boulders at three sites with different topography were first recalculated with GIS-based and then with field data-based shielding factors. For sampling sites in forested low mountainous areas and in high Alpine settings, the shielding factors were stable, i.e. independent of the spatial resolution of the input-elevation data. Vegetation-corrected elevation data allowed more precise shielding factors to be computed for sites in a forested low mountainous area. In most cases, recalculating CRE ages with different shielding factors for the same sampling sites led to minor changes in ages. Only in a few cases, the shifts were in the order of a few percent. It is shown that the use of elevation data with a very high resolution requires precise *xy*-coordinates of sampling sites. Otherwise, there is a risk that small-scale objects in the vicinity of sampling sites will be misinterpreted as topographic barriers. Overall, the toolbox provides an interesting avenue for the determination of shielding factors. Together with the guidelines presented here, it should be more widely used.



25 1 Introduction

The study of glacier fluctuations provides valuable palaeoclimatic information (Mackintosh et al., 2017) if glacier variations are not caused by non-climatic triggers, such as topography (Barr and Lovell, 2014) or surging (Sharp, 1988). Reconstructing glacier variations requires landforms indicative of former glacier extents to be identified and dated. Since the first attempts to use terrestrial cosmogenic nuclides for age determination of moraines (e.g. Brown et al., 1991), cosmic-ray exposure (CRE) dating of moraine boulders has become a well-established technique (Ivy-Ochs et al., 2008; Boxleitner et al., 2019; Hofmann et al., 2019). CRE dating of moraine boulders is based on the principle that spallation reactions, muon-induced reactions and low-energy neutron capture lead to in situ accumulation of cosmogenic nuclides beneath the surface of boulders as soon as they are exposed to cosmic rays (Gosse and Phillips, 2001). Thanks to a rising number of production rate reference sites and joint efforts, particularly the CRONUS Earth and CRONUS-EU projects (Phillips et al., 2016), the accuracy of production rates of cosmogenic nuclides has steadily increased. The determination of the concentration of terrestrial cosmogenic nuclides in rock samples from large boulders on moraines allows for calculating apparent CRE ages of the boulders and, thus, for inferring a minimum age of glacier retreat from these landforms (Briner, 2011).

The production rate at sampling sites depends on the latitude, the altitude, the depth below the rock surface and shielding by topographical obstructions (Ivy-Ochs and Kober, 2008). To take the first two factors into account, scaling schemes, such as the 'Lm' scheme (Nishiizumi et al., 1989; Lal, 1991; Stone, 2000; Balco et al., 2008), have been developed to scale the production rates of reference sites, such as the Chironico landslide (southern Switzerland; Claude et al., 2014), to sampling localities. As the Earth's magnetic field is not constant over time, common age calculators provide the opportunity to correct CRE ages with data from geomagnetic databases (e.g. Muscheler et al., 2005). In addition, the flux of cosmic rays at sampling sites is modified by topographical obstructions, such as mountains (Dunne et al., 1999). Dipping surfaces induce self-shielding from cosmic rays (Gosse and Phillips, 2001). These two types of shielding are considered for calculating a topographic shielding factor. It is commonly reported as dimensionless ratio between 0 and 1: A ratio of 1 means that the sampling site is not altered by topographical obstructions, whereas a ratio of 0 is appropriate for a sampling site completely shielded from cosmic rays (Siame et al., 2000; Balco et al., 2008; Dunai and Stuart, 2009). Common CRE ages calculators, such as the



50 calculator formerly known as the CRONUS Earth calculator (Balco et al., 2008) or the Cosmic Ray Exposure program (CREp; Martin et al., 2017) require this factor as input.

Different methods have been proposed to determine topographic shielding factors. A very common way is to record pairs of azimuths (0-360°) and corresponding elevation angles (0-90°) of characteristic points on the horizon with an inclinometer in
55 the field (cf. Balco, 2018). To determine self-shielding of a dipping surface, strike and dip of the sampling surface are recorded with a geological compass. The pairs of azimuth and elevation angles as well as the strike and dip of the sampling surfaces can be converted in a shielding factor with tools, such as the online calculator available at http://stoneage.ice-d.org/math/skyline/skyline_in.html (last access: 14 January 2022) or the CosmoCalc Microsoft Excel add-in (Vermeesch, 2007). However, this approach is time-consuming and may lead to inconsistencies and uncertainties, as the quality of the
60 calculated shielding factors strongly depend on the experience of the investigator (Li, 2013). Furthermore, bad weather conditions may prevent recording azimuth and elevation angles in the field (Fernández-Fernández et al., 2020).

Codilean (2006) first introduced a geographical information system (GIS)-based approach which enables calculating shielding factors with digital elevation models (DEMs). Li (2013) later implemented this approach in a toolbox for the ESRI ArcGIS
65 software. His toolbox allows for calculating the topographic shielding factor for each cell of the input-raster. As this approach is computationally very inefficient for discrete sampling sites, such as moraine boulders, Li (2018) later developed a second toolbox. He pointed out that calculating shielding factors with his point-based toolbox has several advantages: the approach is less subjective than deriving shielding factors from field measurements, it saves time during fieldwork, elevation data, such as DEMs acquired during the Shuttle Radar Topography Mission (NASA Jet Propulsion Laboratory, 2013), is freely available,
70 and this method is independent of weather conditions during sampling. Since its release, the toolbox has been adopted in several studies on glacier variations (Oliva et al., 2019; Rudolph et al., 2020; Fernández-Fernández et al., 2020; Baroni et al., 2021). Unfortunately, Li (2018) only compared the output of the toolbox with 10 field data-based shielding factors. For validation, he used DEMs acquired during the shuttle radar topography mission (SRTM; Rabus et al., 2003; Farr et al., 2007) with xy -resolutions of 90 and 30 m as well as the High Mountain Asia 8 m-DEM (Shean, 2017). Although the shielding factors



75 derived with the toolbox agreed well with field data-based shielding factors, the validation of the toolbox is not satisfactory
due to the small sample size ($n \ll 30$).

Currently, ^{10}Be CRE dating is being applied to moraines at different localities in the southern Black Forest, Germany. Pairs of
azimuth and elevation angles were recorded at 37 sampling surfaces on moraine boulders during fieldwork in 2019-2021.
80 These data offer the unique opportunity to critically evaluate the output of the toolbox of Li (2018) with a more extensive set
of field data-based shielding factors. Secondly, a high-resolution, vegetation-corrected DEM with a xy -resolution of 1 m is
available for the southern Black Forest. Li (2018) did not test his toolbox with elevation data with such a small pixel size. He
only noted that his toolbox provides stable topographic shielding factors for DEMs with different spatial resolutions. As the
coverage of high-resolution remote sensing data is steadily increasing, this study aims at evaluating whether the use of these
85 data could lead to more accurate shielding factors. This adds supplementary information to the work of Li (2018). As a
geochronologist is mainly interested in the effect of the choice of the shielding factors on CRE ages, three sets of previously
published CRE ages from moraines of different ages (Late Pleistocene, Neoglacial and Little Ice Age) were recalculated with
different shielding factors to provide guidelines for the choice of the input-elevation data for the toolbox.

90 Hence, this research was motivated by the following research questions:

1. Does the output of the ArcGIS toolbox of Li (2018) agree with field data-based topographic shielding factors?
2. Does the spatial resolution of the input-DEM significantly influence the quality of the shielding factors?
3. Does the type of the elevation model (DEM or DSM) have a significant impact on topographic shielding factors?
- 95 4. How large of an impact on the CRE ages do the different methods of determining topographic shielding factors have?



2 GIS-based determination of topographic shielding factors for discrete sampling sites

2.1 Principles of the ArcGIS toolbox and validation

The toolbox requires at least a shapefile with the sampling sites and elevation data (raster). The strike and dip of the sampling surfaces (in degrees) as well as the height above ground of the sampling surfaces (in metres) are optional parameters and can be provided in columns in the attribute table of the shapefile. The name for the field with the GIS-based topographic shielding factors can optionally be defined before running the toolbox (Fig. 1).

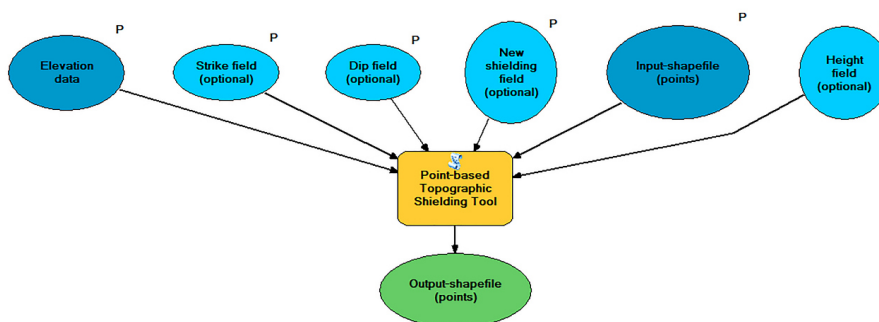


Figure 1: Workflow of the ArcGIS toolbox of Li (2018). The toolbox requires at least elevation data (raster) and the sampling sites (shapefile). The name of the field in the attribute table with the shielding factors can be specified before running the tool. Strike and dip of the sampled surfaces in degrees as well as the height above ground of the sampling surfaces in metres need to be inserted in the attribute table of the input points if one wants to correct the shielding factors for these variables. Parameters in the toolbox are marked with “P”. The Figure was created with the model builder in ArcMap 10.8.1.

The toolbox first retrieves the elevations of the sampling sites from the input-DEM. If provided, the height above ground of the sampling site is added to this elevation. The points are then converted into 3D point features and the calculated elevations of the sampling surfaces serve as z-dimensions. The skyline and skyline graph functions in ArcMap are subsequently applied to obtain horizontal and vertical angles which describe the horizon around each point. The skyline function generates a skyline that represents the farthest visible points along the line of sight around a locality. The increment of the azimuth angle is set to 1° by default. Hence, 360 pairs of azimuth and elevation angles are obtained. Such a high number is normally not ascertained



during fieldwork and, thus, the shielding factors should theoretically be more accurate than those derived from field measurements. The skyline graph function then exports horizontal and vertical angles of the points on the skyline for these azimuth angles.

120 To take the shielding of a dipping surface into account, the range of azimuths (360°) are divided into 1° increments and the elevation angle (θ) is calculated for each azimuth according to the following equation:

$$\theta = \arctan[\tan \theta_d \cos(\varnothing - \varnothing_s)], \quad (1)$$

125 where θ_d and \varnothing_s are the dip and strike of the dipping surface, respectively. \varnothing is the azimuth. Hence, the approach of Li (2018) is identical to the 'skyline.m' MATLAB function implemented in the common topographic shielding calculator of Balco (2018).

The values calculated with to Eq. (1) are compared with the azimuth and elevation angles derived with the skyline and skyline graph functions. Again, this approach is identical to that in the topographic shielding calculator mentioned above. The larger
130 of the two values is used for determining the topographic shielding factor according to the equation of Dunne et al. (1999):

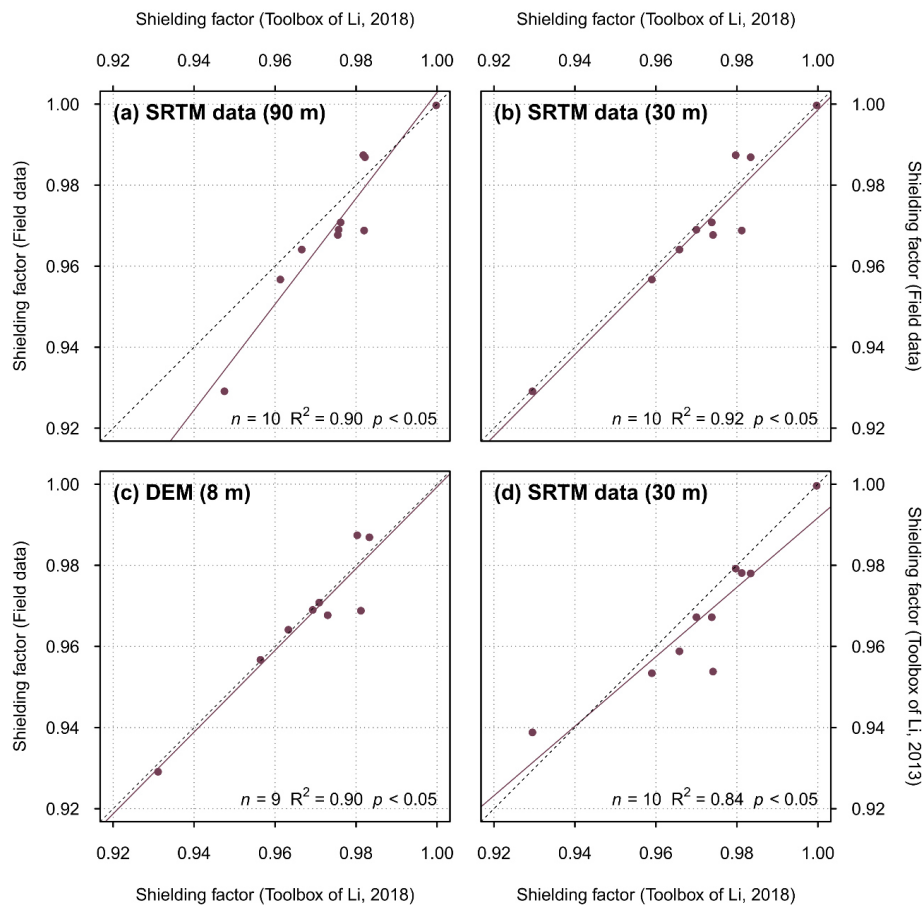
$$C_T = 1 - \sum_{i=1}^n \Delta\varnothing_i \sin^{m+1}(\theta_i), \quad (2)$$

where C_T is the topographic shielding factor, n stands for the number of topographic obstructions, \varnothing_i and θ_i are the azimuth and elevation angles, respectively, associated with each topographical obstruction and m is an empirical constant. For the latter, an
135 empirical value of 2.3 is commonly used (Nishiizumi et al., 1989; Gosse and Phillips, 2001; Balco et al., 2008).

Li (2018) validated his toolbox by comparing shielding factors computed with his toolbox with shielding factors derived from field measurements for boulders in the Urumqi catchment in Tian Shan, China. He used SRTM data with xy -resolutions of 90 and 30 m as well as the High Mountain Asia 8 m-DEM (Shean, 2017) as input-elevation data. The topographic shielding
140 factors agree generally with the field data-based shielding factors (Fig. 2). The use of SRTM data with a xy -resolution of about



30 m resulted in the best fit (Fig. 2a). In addition, he compared the output of his new toolbox with that of an older toolbox (Li, 2013). Both toolboxes yielded similar results ($R^2 = 0.84$; $p < 0.05$; Fig. 2d).



145 **Figure 2: Topographic shielding factors for 10 sampling locations in the Urumqi catchment in Tian Shan, China, computed with (a) SRTM data, (b) SRTM elevation data with a higher spatial resolution and (c) with the High Mountain Asia DEM (Shean, 2017) versus field data-based topographic shielding factors. Note that one sampling site is not covered by the High Mountain Asia 8 m-DEM and, thus, the topographic shielding factor was only determined for nine boulders (Li, 2018). (d) Topographic shielding factors determined with the toolbox of Li (2018) versus the topographic shielding factors derived with an older toolbox (Li, 2013). The strike,**



150 **dip and height of the sampling surfaces above ground were set to zero in the new toolbox, as the older one does not takes these variables into account (Li, 2018). All correlations are statistically significant when choosing $\alpha = 0.05$ as significance level. The solid and dotted lines are the linear models and 1:1 lines, respectively. The numbers in parentheses refer to the spatial resolution of the elevation data. Data from Li (2018).**

155 **2.2 Application in previous studies**

According to a literature search in Scopus on the 8th of February 2022, Li's 2018 ArcGIS toolbox has been adopted in 16 studies to compute topographic shielding factors for a range of different sampling surfaces, such as polished bedrock or boulders on moraines. As can be seen in Table 1, the toolbox has mainly been applied in studies in the field of glacial geomorphology. From 0.5 to 30 m, the *xy*-resolutions of the input-DEMs was very heterogenous (Table 1). The reason for the application of the toolbox was only stated in some of the original publications. Cardinal et al. (2021) selected the toolbox because recording pairs of azimuth and elevation angles at sampling surfaces on gorge walls proved to be impossible. Hofmann et al. (2022) were unable to record the elevations of the horizon during sampling of a moraine boulder due to the location of sampling sites in dense forests. Oliva et al. (2019) used the toolbox for the calculation of shielding factors for sites where unreliable field data were recorded. Fernández-Fernández et al. (2020), Palacios et al. (2021) and Tanarro et al. (2021) selected the approach of Li (2018), as cloudiness or fog prevented recording azimuth and elevation angles in the field. The shielding factors were considered valid in previous publications. To the best knowledge of the author, the effect on the input-DEM has only been briefly discussed in one publication (Cardinal et al., 2021). Cardinal et al. (2021) noted that the shielding factors may be misleading if small topographic anomalies, such as boulders, are present in the vicinity of sampling sites that lead to partial shielding of cosmic rays.

170

Table 1: Application of the ArcGIS toolbox of Li (2018) in previous studies.

Reference	Type of the sampling site	<i>xy</i> -resolution of the input-elevation data (m)
Baroni et al. (2021)	Moraine boulders	Not specified



Cardinal et al. (2021)	Gorge walls	0.5
Dong et al. (2020)	Moraine boulders	30
Fernandes et al. (2021)	Erratic boulders, moraine boulders and glacially polished bedrock	5
Fernandes et al. (2022)	Glacially polished bedrock and moraine boulders	5
Fernández-Fernández et al. (2020)	Glacially polished bedrock, moraine boulders, boulders on rock glaciers and boulders of debris-covered glaciers	Not specified
Hofmann et al. (2022)	Moraine boulders	30
Mohren et al. (2020)	Bedrock knickpoints	1
Oliva et al. (2019)	Moraine boulders	Not specified
Oliva et al. (2021)	Moraine boulders, boulders of a debris-covered glacier, glacially polished bedrock and an erratic boulder	Not specified
Palacios et al. (2021)	Moraine boulders and boulders of rock glaciers	Not specified
Peng et al. (2020)	Moraine boulders	30
Rudolph et al. (2020)	Deglaciated bedrock and moraine boulders	1
Santos-González et al. (2022)	Boulders of a rock glacier and a debris avalanche	Not specified



Tanarro et al. (2021)	Erratic boulders, moraine boulders as well as boulders of a former debris-covered glacier and of a rock glacier	0.5
Valentino et al. (2021)	Erratic boulders, moraine boulders and glacially polished bedrock	10

3 Data and methods

3.1 Determination of topographic shielding factors for moraine boulders in the southern Black Forest

3.1.1 Fieldwork

175 The skyline around the boulders was described by recording pairs of azimuth and elevation angles, as proposed by Balco
(2018). Azimuth and elevation angles were measured with a handheld Suunto Tandem/360PC/360R G inclinometer
(uncertainty: 0.25°). The dip and strike of the sampling surfaces were measured with a geological compass (uncertainty: 5°).
See the Tables S1 to S74 for field data. To determine the location of the boulders in the southern Black Forest as precisely as
possible, a global navigation satellite system (Leica CS20 controller and Leica Viba GS14 antenna) was selected for
180 determining *xy*-coordinates (Table S75).

3.2.1 Conversion into shielding factors with an online calculator

Dip directions were subsequently converted into strike angles. Topographic shielding factors were ultimately computed by
entering strike and dip values as well as the azimuth and corresponding elevation angles in Balco's online topographic shielding
calculator.

185 3.2 GIS-based calculation of topographic shielding factors

For the first step, a shapefile of the sampling sites with the strike, dip and height above ground of the sampling surfaces was
created in the ESRI ArcMap software (version: 10.8.1).



To answer whether the type of elevation data (corrected for vegetation or not) has an influence on the fit between topographic
190 shielding factors and field data-based shielding factors, common DEMs were tested. Firstly, freely available void-filled SRTM
data with a xy -resolution of about 30 m at the equator (referred to the WGS84 ellipsoid; NASA Jet Propulsion Laboratory,
2013) were selected. These data have a relative vertical absolute height error of <10 m at 90% confidence interval (Rodríguez
et al., 2006). Secondly, elevation data with a xy -resolution of 12 m at the equator (referred to the WGS84 ellipsoid) acquired
during the TerraSAR-X add-on for Digital Elevation Measurement (TanDEM-X) mission (Krieger et al., 2007) were obtained
195 from the German Aerospace Centre (DLR; DLR, 2016). The relative vertical height accuracy of the DEMs is 2 and 4 m for
low (slope $<20^\circ$) and high (slope $>20^\circ$) relief terrain, respectively, at 90% confidence interval (Rizzoli et al., 2017). Thirdly,
a high-resolution DEM of the southern Black Forest with a xy -resolution of 1 m was selected for this study. This elevation
model has a vertical accuracy of 0.5 m.

200 As mentioned in Sect. 2.1, the toolbox offers the opportunity to take the height of the sampled boulders into account. To assess
whether this height correction enables determining more precise shielding factors, topographic shielding factors were corrected
in a second run.

To evaluate whether the GIS-based shielding factors depend on the spatial resolution of the input-elevation data, the high-
205 resolution DEM of the southern Black Forest with a xy -resolution of 1 m was resampled to xy -resolutions of 12 and 30 m via
bilinear interpolation in ArcMap 10.8.1 to allow for comparisons with SRTM and TanDEM-X elevation data, respectively.
The toolbox was then run with the shapefiles and the resampled raster files. The shielding factors were corrected for the boulder
height.

3.2 Determination of topographic shielding factors for moraine boulders in high Alpine settings

210 As outlined in the previous section, shielding factors for moraine boulders in the southern Black Forest were calculated with
a high-resolution DEM and two resampled versions of the DEM to test whether the shielding factors are sensitive to the spatial
resolution of the input-elevation data. The southern Black Forest is a low mountainous area and, therefore, the result of this
sensitivity test may not be representative for high Alpine settings where many geomorphologists work.



215 To elucidate this question in further detail, shielding factors for previously dated boulders on Neoglacial moraines in the
forefield of a glacier in Switzerland, the Steingletscher (Fig. 3; Schimmelpfennig et al., 2014) were calculated with a high-
resolution light detection and ranging (LiDAR)-based DEM (swissALTI^{3D}; available at:
<https://www.swisstopo.admin.ch/de/geodata/height/alti3d.html>, last access: 19 May 2022). To ensure comparability, this DEM
was resampled to xy -resolutions of 1, 12 and 30 m with bilinear interpolation in ArcMap 10.8.1. In addition, shielding factors
220 were computed with SRTM and TanDEM-X elevation data. The Écrins massif (westernmost Alps; Fig. 3) was chosen as a
third site. Moraines in forefield of several glaciers, the Bonnepierre, Etages, Lautaret and Rateau glaciers, have already been
dated and their ages fall into the Neoglacial (Le Roy et al., 2017). As TanDEM-X data did not cover the sites in the Écrins
massif, shielding factors were only calculated with SRTM data with a xy -resolution of 30 m.

225

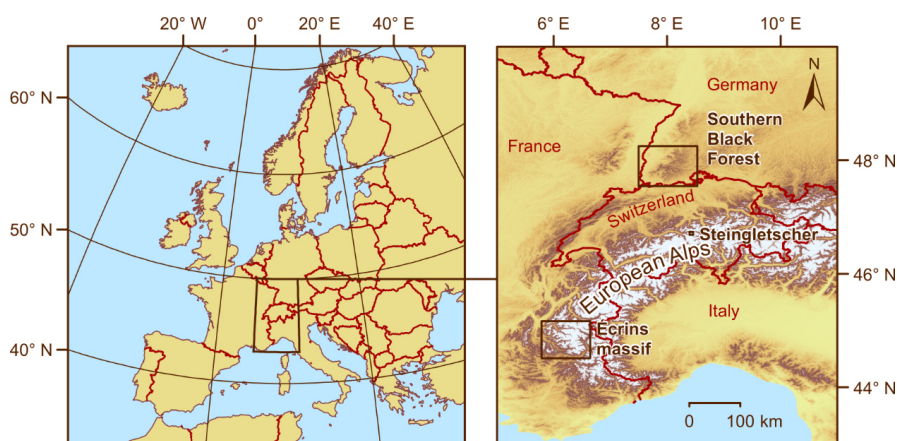


Figure 3: Location of the sites chosen for the sensitivity experiments. The first site, the Black Forest, lies in the south-western part of Germany close to the border to France and Switzerland. The second site, the Écrins massif, is located in the westernmost European Alps, whereas the third site, the forefield of Steingletscher, is situated in the central Alps further NE. SRTM data (NASA Jet Propulsion Laboratory, 2013) were used to create the map on the right side. © EuroGeographics for the administrative boundaries.

230



3.4 Recalculation of CRE ages

To assess the effect of the different methods for deriving shielding factors on CRE ages, three tests were performed. As they aim at assessing the effect on CRE ages, they are hereinafter referred to as sensitivity experiments.

235 The first sensitivity test aimed to assess the effect of the different methods for calculating topographic shielding factors on CRE ages of boulders in mountains with an intermediate elevation that have been exposed to cosmic radiation since the Late Pleistocene. Boulders on terminal moraines in a formerly glaciated valley (Sankt Wilhelmer Tal) in the southern Black Forest (Germany; Fig. 3) were chosen. See Hofmann et al. (2022) for a description of the study site and for an interpretation of the ages.

240

The second sensitivity experiment aimed to determine whether the choice of topographic shielding factors has a significant impact on the CRE ages of surfaces that have been exposed for the last few millennia. Boulders on terminal moraines in the forefield of the four glaciers in the Écrins massif were chosen. Although the ^{10}Be production rates at the sampling sites are much higher than in the southern Black Forest due to the higher elevation, the in-situ accumulated ^{10}Be concentrations in the
245 sampled boulders are lower due to relatively short durations of exposure. See Le Roy et al. (2017) for a description of the sites in the Écrins massif and for an interpretation of the ages.

As CRE dating has also been applied to terminal moraines of only a few centuries in age (e.g. Schaefer et al., 2009 or Braumann et al., 2020), boulders on Little Ice Age (LIA) and post-LIA terminal moraines of Steingletscher, Switzerland (Fig. 3), were
250 chosen for the third sensitivity experiment. These ages and the study site are presented in Schimmelpfennig et al. (2014). The ^{10}Be concentration in samples from 14 of 16 boulders amounts to less than 10,000 atoms ^{10}Be g^{-1} quartz due to short durations of exposure.



255 As only SRTM data covered all sites, CRE ages were first recalculated with SRTM data-based shielding factors and then with
field-data based shielding factors. CRE ages were recalculated with the CREp program (Martin et al., 2017) and the following
parameters: time-dependent ‘Lm’ scaling (Nishiizumi et al., 1989; Lal, 1991; Stone, 2000; Balco et al., 2008), the ERA40
atmosphere model (Uppala et al., 2005), the atmospheric ^{10}Be -based geomagnetic database of Muscheler et al. (2005), the
density of quartz as sample density (2.65 g cm^{-3}) and the ^{10}Be production rate derived from rock samples from the Chironico
260 landslide (southern Switzerland; Claude et al., 2014). If these parameters are chosen in CREp, the ^{10}Be production rate at sea-
level and high latitudes amounts to $4.10 \pm 0.10 \text{ atoms g}^{-1} \text{ quartz}$. The calculator provides CRE ages in kiloyears before 2010 CE
rounded to the nearest decade.

3.5 Statistical analysis

The statistical analysis of the output of the toolbox was performed with the R software (version 4.0.5; R Core Team, 2021)
265 and R Studio (version 1.4.1106; RStudio Team, 2021). Relationships between the GIS-based topographic shielding factors and
those derived from field measurements were assessed by computing the Pearson product-moment correlation coefficient and
the coefficient of determination (R^2). Linear models were considered statistically significant when the calculated p -value was
lower than the common significance level of $\alpha = 0.05$. It should be noted that this common value is a convention and therefore
arbitrary. See Dormann (2020, and references therein) for further discussion.

270 4 Results

4.1 Topographic shielding factors for moraine boulders

SRTM data-based shielding factors for moraine boulders in the southern Black Forest, the Écrins massif and in the forefield
of Steingletscher ($n = 77$) were strongly correlated with the field-data based shielding factors ($R^2 = 0.89$; $p < 0.05$; Fig. 4a).
Considering the boulder height during topographic shielding factor calculations led to a slightly stronger agreement ($R^2 = 0.90$;
275 $p < 0.05$; Fig. 4b).

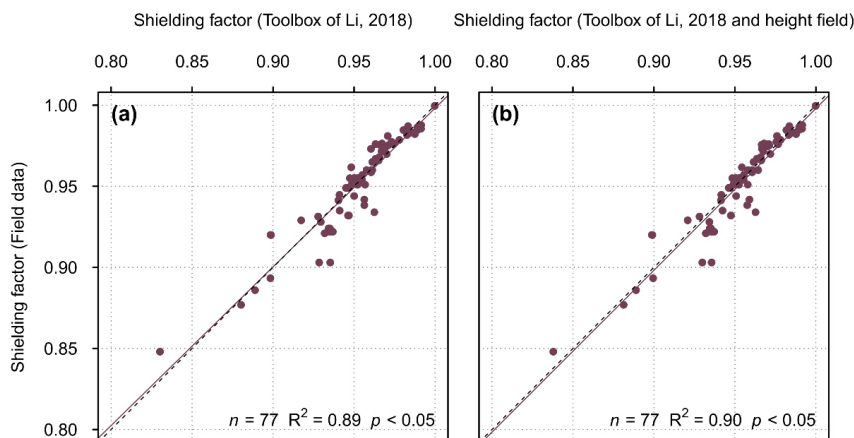
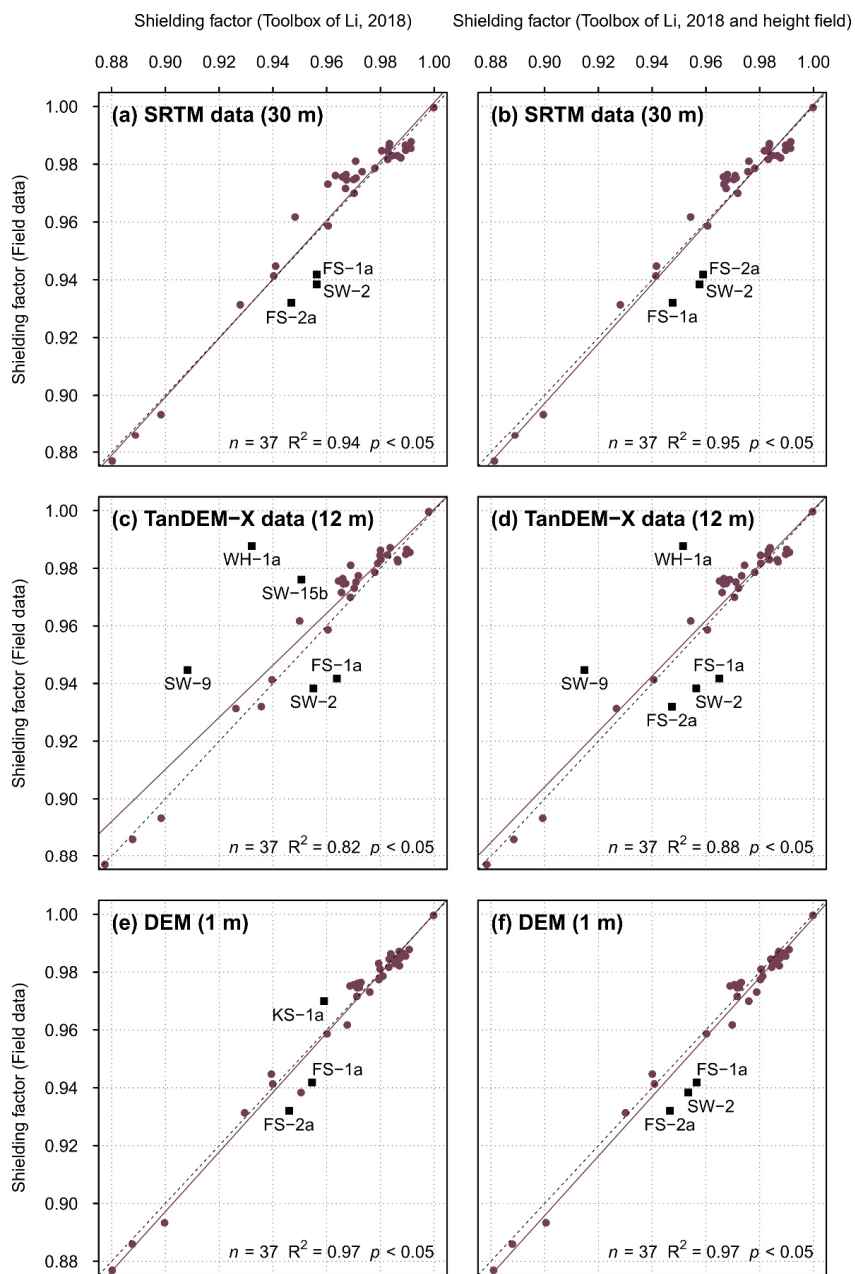


Figure 4: (a) Shielding factors for moraine boulders in the southern Black Forest, the Écrins massif and in the forefield of Steingletscher determined with SRTM elevation data versus field data-based shielding factors. (b) the same as (a), but the shielding factors were corrected for the boulder height. For field data-based shielding factors for boulders in the Écrins massif and in the forefield of Steingletscher, see Le Roy et al. (2017) and Schimmelpennig et al. (2014), respectively.

4.1.1 Southern Black Forest

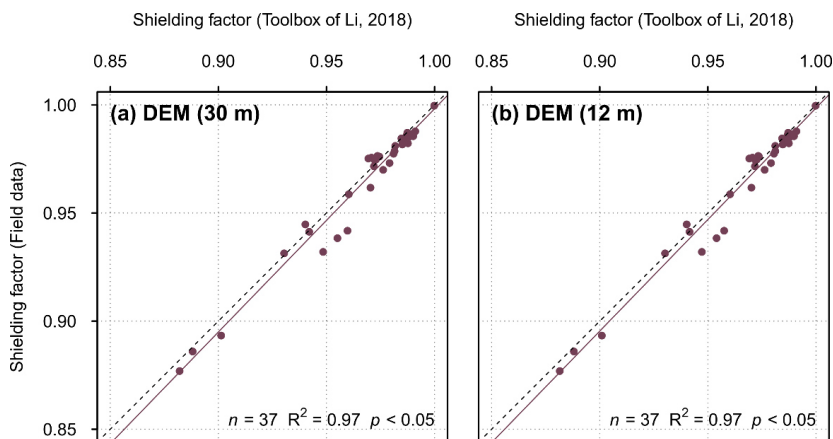
SRTM data-based shielding factors were generally consistent with those derived from field data ($R^2 = 0.94$; $p < 0.05$; Fig. 5a). As can be seen in Fig. 5a, only the shielding factors for the FS-1a, FS-2a and SW-2 boulders did not match. Incorporating the boulder height during shielding factor calculations with SRTM data led to a slightly stronger agreement ($R^2 = 0.95$; $p < 0.05$; Fig. 5b). The correlation between the TanDEM-X data-based shielding factors and the field-data based shielding factors was weaker ($R^2 = 0.82$; $p < 0.05$; Fig. 5c). The discrepancy was largest for the FS-1a, SW-2, SW-9 and WH-1a boulders (Fig. 5c). Incorporating the boulder height led to inconsistent shielding factors for the FS-1a, FS-2a, SW-2, SW-9 and WH-1a boulders (Fig. 5d). Shielding factors determined with the high-resolution DEM were most consistent with field-data based shielding factors ($R^2 = 0.97$; $p < 0.05$; Fig. 5e & f). The offset between the shielding factors predicted by the linear model and those computed with the calculator of Balco (2018) was largest for the FS-1a, FS-2a and KS-1a boulders and for the FS-1a, FS-2a and SW-2 boulders when the height of the boulders was taken into account, respectively (Fig. 5e & f).



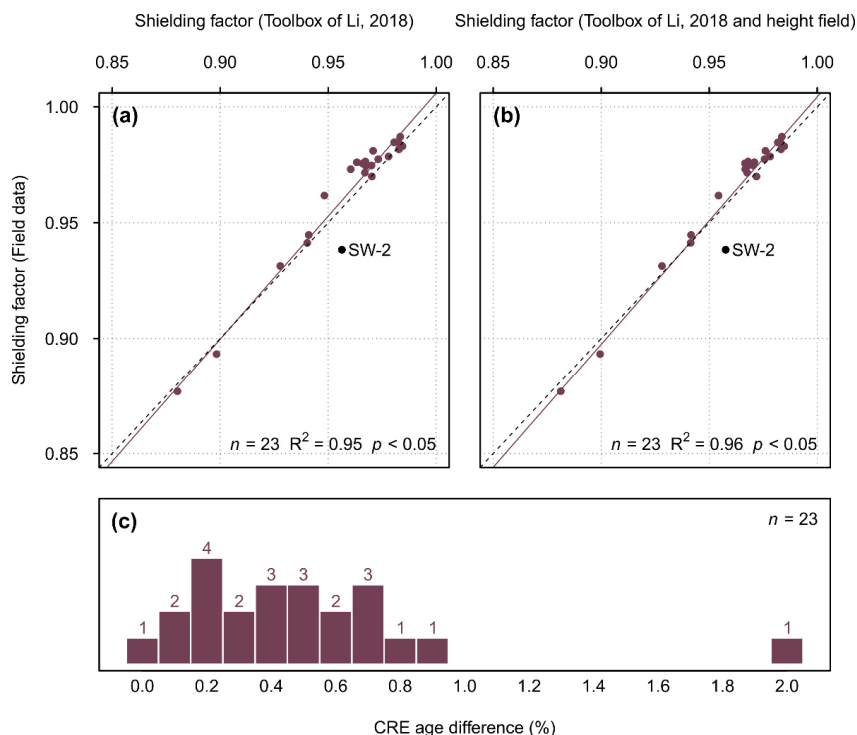


295 **Figure 5:** (a) Topographic shielding factors for boulders in the southern Black Forest determined with the ArcGIS toolbox of Li
(2018) and SRTM elevation data (NASA Jet Propulsion Laboratory, 2013) versus those derived from field data. (b) the same as (a),
but with a correction for the boulder height. (c) Topographic shielding factors calculated with the ArcGIS toolbox and a TanDEM-
X-DEM versus those derived from field measurements. (d) the same as (c), but the shielding factors were corrected for the boulder
height. (e) Topographic shielding factors calculated with the ArcGIS toolbox and a high-resolution DEM versus those derived from
300 field measurements. (f) the same as (e), but with a correction for the boulder height. Outliers are marked with dark-red squares.
Linear models and 1:1 lines are marked with solid and dashed lines, respectively. The numbers in parentheses refer to the spatial
resolution of the elevation data.

The correlation between GIS-based shielding factors and field data-based shielding factors remained unchanged when
305 resampled versions of the high-resolution DEM were chosen as input ($R^2 = 0.97$; $p < 0.05$; Fig. 6). GIS-based shielding factors
for the boulders selected for the first sensitivity experiment were very consistent with the field data-based shielding factors (R^2
 $= 0.95$ and 0.96 ; $p < 0.05$; Fig. 7). For individual shielding factors, see Tables S75 & S76.



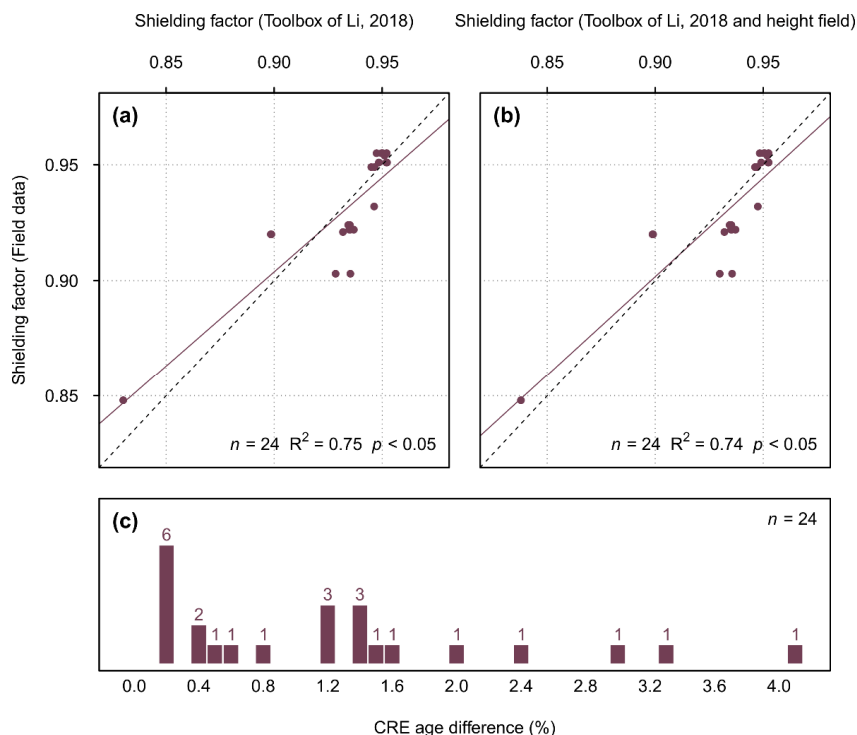
310 **Figure 6:** (a) Shielding factors determined with the toolbox and a resampled version of the high-resolution DEM (spatial resolution:
30 m) versus field data-based shielding factors. (b) GIS-based shielding factors determined with a resampled version of the high-
resolution DEM (spatial resolution: 12 m) versus field data-based shielding factors.



315 **Figure 7: (a) Topographic shielding factors for boulders on moraines in the southern Black Forest (Hofmann et al., 2022) derived from field data versus those determined with the ArcGIS toolbox (Li, 2018) and SRTM elevation data (NASA Jet Propulsion Laboratory, 2013). (b) The same as (a), but the shielding factors determined with the toolbox were corrected for the boulder height. (c) Histogram of CRE age differences (given in per cent with respect to the ages determined with the field-based shielding factors).**

320 4.1.2 Écrins massif

The fit between the GIS-based shielding factors and those derived from field data turned out to be lower than for boulders in the southern Black Forest ($R^2 = 0.75$; $p < 0.05$; Fig. 8a). Incorporating the boulder height led to a slightly lower agreement ($R^2 = 0.74$; $p < 0.05$; Fig. 8b). See Table S77 for individual shielding factors.



325

Figure 8: (a) Topographic shielding factors for boulders on moraines in the Écrins massif (Le Roy et al., 2017) derived from field data versus those determined with the ArcGIS toolbox (Li, 2018) and SRTM elevation data (NASA Jet Propulsion Laboratory, 2013). (b) The same as (a), but the shielding factors determined with the toolbox are corrected for the boulder height. (c) Histogram of CRE age differences (given in per cent with respect to the ages determined with the field-based shielding factors).

330

4.1.3 Steingletscher

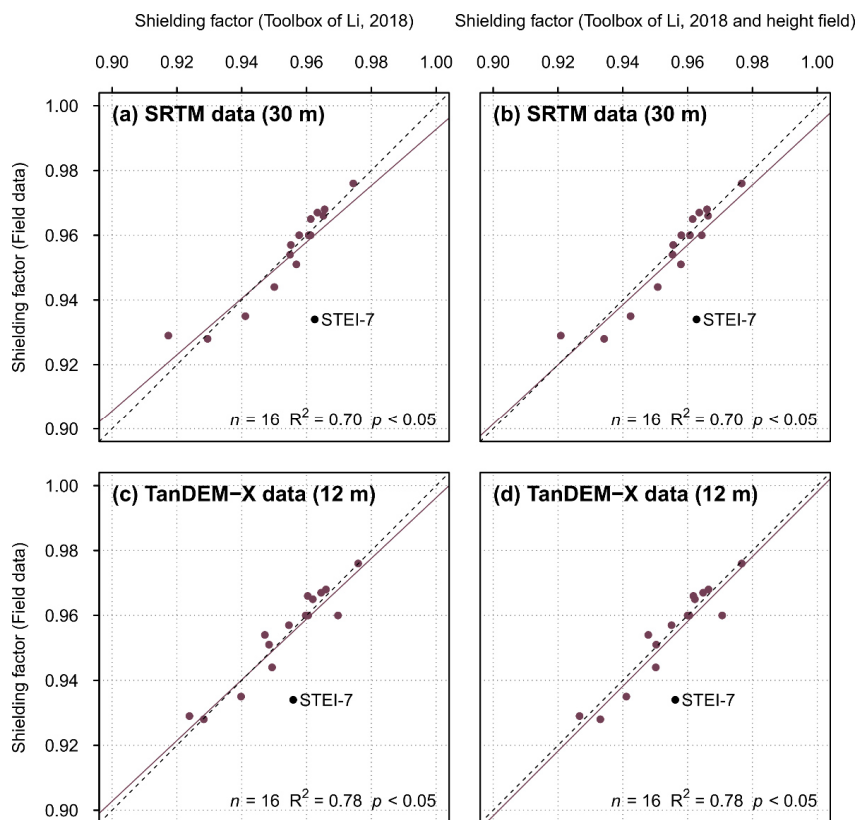
Generally, SRTM data-based shielding factors for moraine boulders in the forefield of Steingletscher were consistent with field data-based shielding factors ($R^2 = 0.70$; $p < 0.05$; Fig. 9a & b). The use of TanDEM-X elevation data led to a better fit between the shielding factors ($R^2 = 0.78$; $p < 0.05$; Fig. 9c & d). Shielding factors calculated with a high-resolution DEM (swissALTI^{3D}) with a xy -resolution of 1m and field data-based shielding factors were less consistent ($R^2 = 0.70$; $p < 0.05$; Fig. 10c). The use of resampled versions of the DEM with spatial resolutions of 30 and 12 m led to a similar fit between the

335



shielding factors ($R^2 = 0.71$ and $R^2 = 0.70$, respectively; Fig. 10a, b). Irrespective of the input-DEM, GIS-based shielding factors for the STEI-7 boulder did not match the field data-based shielding factor (Fig. 9). Individual shielding factors are given in the supplement (Tables S78 & S79).

340



345 **Figure 9:** (a) Topographic shielding factors for moraine boulders in the forefield of Steingletscher (Schimmelpfennig et al., 2014) determined with the ArcGIS toolbox and SRTM data versus field-data based shielding factors. (b) The same as (a), but the shielding factors were corrected for the boulder height. (c) Topographic shielding factors computed with the toolbox and TanDEM-X elevation data versus field data-based shielding factors for the same boulders. (d) The same as (c), but the shielding factors were corrected for the boulder height.

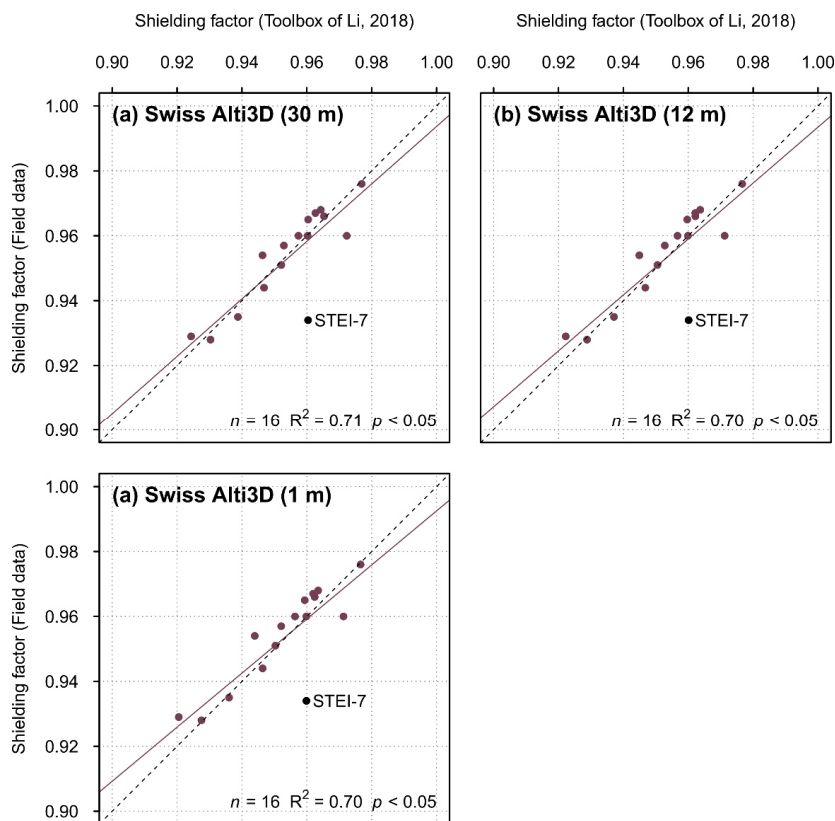


Figure 10: Topographic shielding factors for moraine boulders in the forefield of Steingletscher determined with resampled versions of a LiDAR-based DEM (Swiss ALTI^{3D}) with *xy*-resolutions of (a) 30, (b) 12 and (c) 1 m.

350

4.2 Sensitivity tests

The results of the first sensitivity experiment are presented in Table 2 and in Fig. 7. CRE ages determined with field data-based shielding factors differed, on average, by 67 years from CRE ages computed with SRTM data-based shielding factors. With respect to the age determined by field data-based shielding factors, the CRE age difference was, on average, 0.5%. The



355 maximum CRE age difference amounted to 280 years or 2.0% (Table 2). As can be seen in Fig. 7c, the CRE age difference
 for most of the sampled boulders turned out to be less than one per cent.

360 **Table 2: CRE ages of boulders on moraines in Sankt Wilhelmer Tal. The ages have already been presented and interpreted elsewhere (Hofmann et al., 2022). They were first calculated with the CREp program (Martin et al., 2017) with topographic shielding factors derived from field measurements and then with topographic shielding factors calculated with the ArcGIS-toolbox of Li (2018) and SRTM elevation data (NASA Jet Propulsion Laboratory, 2013).**

Boulder name	CRE age (shielding factor derived from field measurements; a before 2010 CE)	CRE age (shielding factor calculated with the ArcGIS toolbox; a before 2010 CE)	CRE age difference (a)	CRE age difference with respect to the CRE age calculated with the field data-based shielding factor (%)
KS-1a	14260±560	14220±560	40	0.3
KS-1b	4240±380	4270±380	30	0.7
KS-2a	10320±510	10380±510	60	0.6
KS-2b	12880±660	12900±650	20	0.2
KS-2d	13470±660	13520±660	50	0.4
KS-2e	14780±650	14790±650	10	0.1
KS-2f	8720±510	8730±510	10	0.1
KS-2g	12110±630	12090±620	20	0.2
KS-3a	13990±680	14020±690	30	0.2
SW-10	15680±870	15740±880	60	0.4
SW-11a	17310±990	17430±1000	120	0.7
SW-11b	9840±450	9880±460	40	0.4



SW-11c	14940±800	15070±810	130	0.9
SW-11d	17440±980	17500±980	60	0.3
SW-12a	16820±710	16960±710	140	0.8
SW-15a	16220±700	16300±700	80	0.5
SW-15b	17320±670	17410±670	90	0.5
SW-16	3510±310	3490±320	20	0.6
SW-18a	19960±1000	19830±990	130	0.7
SW-18b	17470±750	17470±760	0	0.0
SW-18c	16930±790	16850±790	80	0.5
SW-2	14260±830	13980±820	280	2.0
SW-9	16050±740	16090±740	40	0.2

The results of the second sensitivity experiments are presented in Table 3 and in Fig. 8. CRE ages determined with the shielding factors from field data differed, on average, by 35 years from those computed with the GIS-based shielding factors. This is equivalent to an average CRE age difference of 1.2% with respect to the CRE age determined with field data-based topographic shielding factor. The maximum CRE age difference amounted to 4.1% or 120 years (Table 3). For most of the sampled boulders, the CRE age difference amounted to 40 years (1.6 %) or less (Fig. 8).

Table 3: Recalculated CRE ages of boulders on terminal moraines of the Rateau (RAT), Lautaret (LAU), Bonnepierre (BON) and Etages (ETA) glaciers in the Écrins massif (Le Roy et al., 2017). In the CREp program (Martin et al., 2017), the CRE ages were first calculated with topographic shielding factors derived from field measurements (presented in Le Roy et al., 2017) and subsequently with topographic shielding factors calculated with the ArcGIS-toolbox of Li (2018) and SRTM elevation data (NASA Jet Propulsion Laboratory, 2013).



Boulder name	CRE age (shielding factor derived from field measurements; a before 2010 CE)	CRE age (shielding factor calculated with the ArcGIS toolbox; a before 2010 CE)	CRE age difference (a)	CRE age difference with respect to the CRE age calculated with the field-data based shielding factor (%)
RAT01	2650±190	2610±190	40	1.5
RAT02	2430±190	2400±190	30	1.2
RAT04	3370±240	3330±230	40	1.2
RAT05	2450±210	2410±200	40	1.6
RAT06	2950±350	2910±340	40	1.4
RAT07	3330±240	3290±240	40	1.2
RAT08	3590±370	3470±360	120	3.3
RAT09	4130±490	4030±470	100	2.4
RAT10	2910±570	2870±570	40	1.4
LAU01	1500±210	1530±210	30	2.0
BON00	4170±490	4180±490	10	0.2
BON02	4910±290	4940±290	30	0.6
BON03	5220±540	5260±540	40	0.8
BON04	4860±450	4790±440	70	1.4
BON05	4130±300	4140±310	10	0.2
BON06	4200±290	4210±290	10	0.2
BON07	4170±380	4160±380	10	0.2
BON08	2510±400	2520±400	10	0.4
BON09	2380±260	2390±260	10	0.4
BON10	4030±260	4050±260	20	0.5



BON11	6260±750	6270±750	10	0.2
BON12	4770±420	4760±420	10	0.2
ETA01	980±180	1020±180	40	4.1
ETA02	1000±160	1030±170	30	3.0

375

The results of the third sensitivity experiments are presented in Table 4. Table 4 reveals that the CRE ages derived with GIS-based shielding factors are indistinguishable from those computed with field data-based shielding factors. For two boulders, the CRE age difference turned out to be 10 years. Although the shielding factors for the STEI-7 boulder do not agree, the CRE age of the boulder remained unchanged.

380

Table 4: Recalculated CRE ages of moraine boulders in the forefield of Steingletscher (Switzerland; Schimmelpfennig et al., 2014). In the CREp program (Martin et al., 2017), CRE ages were first calculated with topographic shielding factors derived from field measurements (presented in Schimmelpfennig et al., 2014) and then with topographic shielding factors calculated with the ArcGIS-toolbox of Li (2018) and SRTM elevation data (NASA Jet Propulsion Laboratory, 2013).

Boulder name	CRE age (shielding factor derived from field measurements; a before 2010 CE)	CRE age (shielding factor calculated with the ArcGIS toolbox; a before 2010 CE)	CRE age difference (a)	CRE age difference with respect to the CRE age calculated with the field-data based shielding factor (%)
STEI-12-23	580±50	580±50	0	0.0
STEI-23	530±20	530±20	0	0.0
STEI-12-13	530±30	530±30	0	0.0
STEI-26	470±30	460±30	10	2.1
STEI-12-05	360±30	360±30	0	0.0
STEI-12-14	340±40	350±40	10	2.9
STEI-18	300±20	300±20	0	0.0



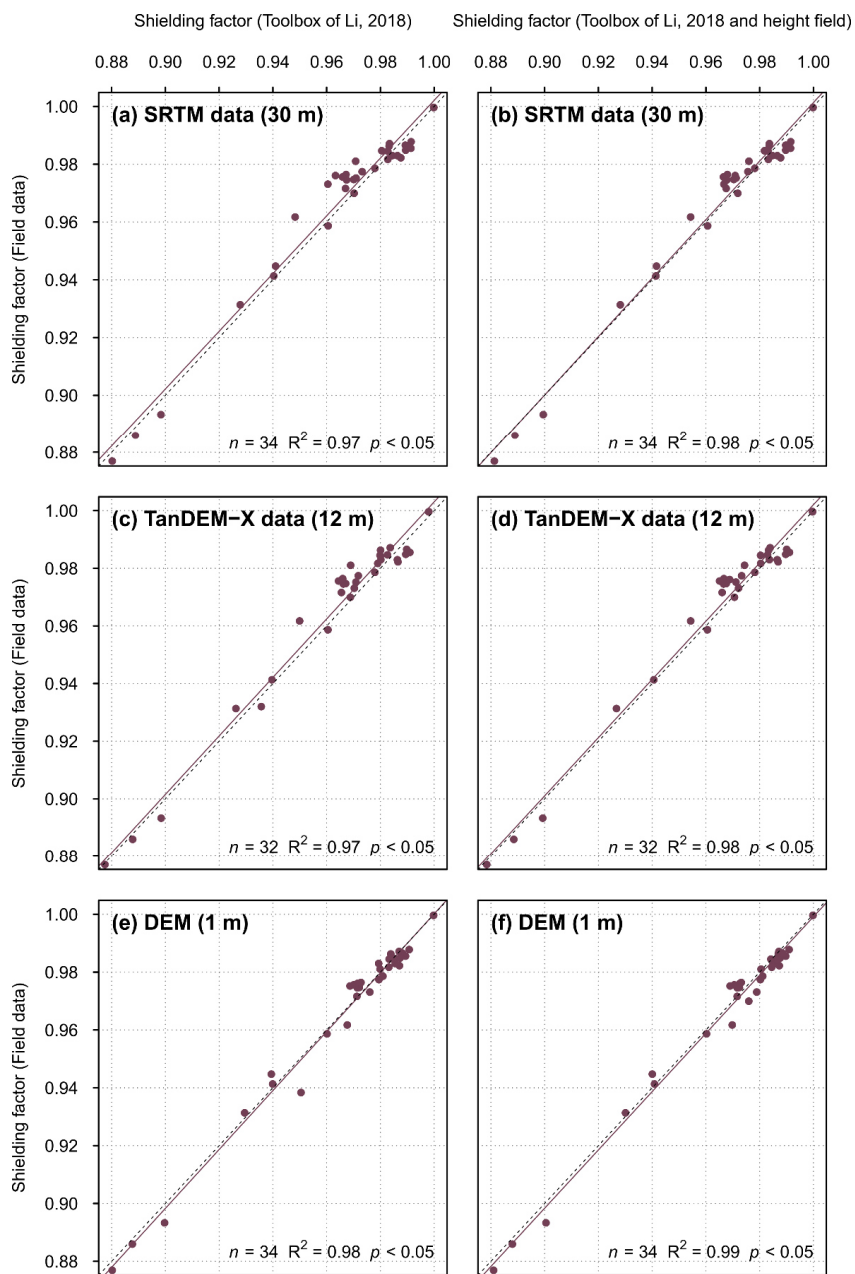
STEI-15	270±10	270±10	0	0.0
STEI-12-21	260±20	260±20	0	0.0
STEI-12-11	240±20	240±20	0	0.0
STEI-12-07	200±30	190±30	10	5.0
STEI-12-04	190±20	190±20	0	0.0
STEI-17	190±10	190±10	0	0.0
STEI-12-20	140±40	140±40	0	0.0
STEI-16	150±10	150±10	0	0.0
STEI-7	120±10	120±10	0	0.0

385 5 Discussion

5.1 Explanations for mismatching shielding factors

As highlighted in Fig. 5b, SRTM data-based shielding factors for the FS-1a, FS-2a and FS-3a boulders in the southern Black Forest did not match field-data based shielding factors. Since the boulders were situated in densely forested areas, measuring pairs of azimuth and elevation angles proved difficult during fieldwork. The horizon around the sampling sites was only partly visible. As the farthest visible points were situated on forested mountains, determining precise elevation angles of the terrain surface turned out to be challenging and, hence, the field-data based shielding factors for these boulders may not be reliable.

Figure 5b reveals that the SRTM-based shielding factors for the FS-1a, FS-2a and SW-2 boulders turned out to be systematically higher than the field data-based shielding factors. This observation raises the question whether the discrepancy could also be due to the lack of a correction for vegetation cover in SRTM data. This explanation is, however, unlikely: the use of the vegetation-corrected DEM led to similar shielding factors for these boulders. Excluding the potentially “problematic” shielding factors for the FS-1a, FS-2a and SW-2 boulders leads to a better fit between the shielding factors (Fig. 11b).





400 Figure 11: The same as Figure 4, but without potentially “problematic” shielding factors.

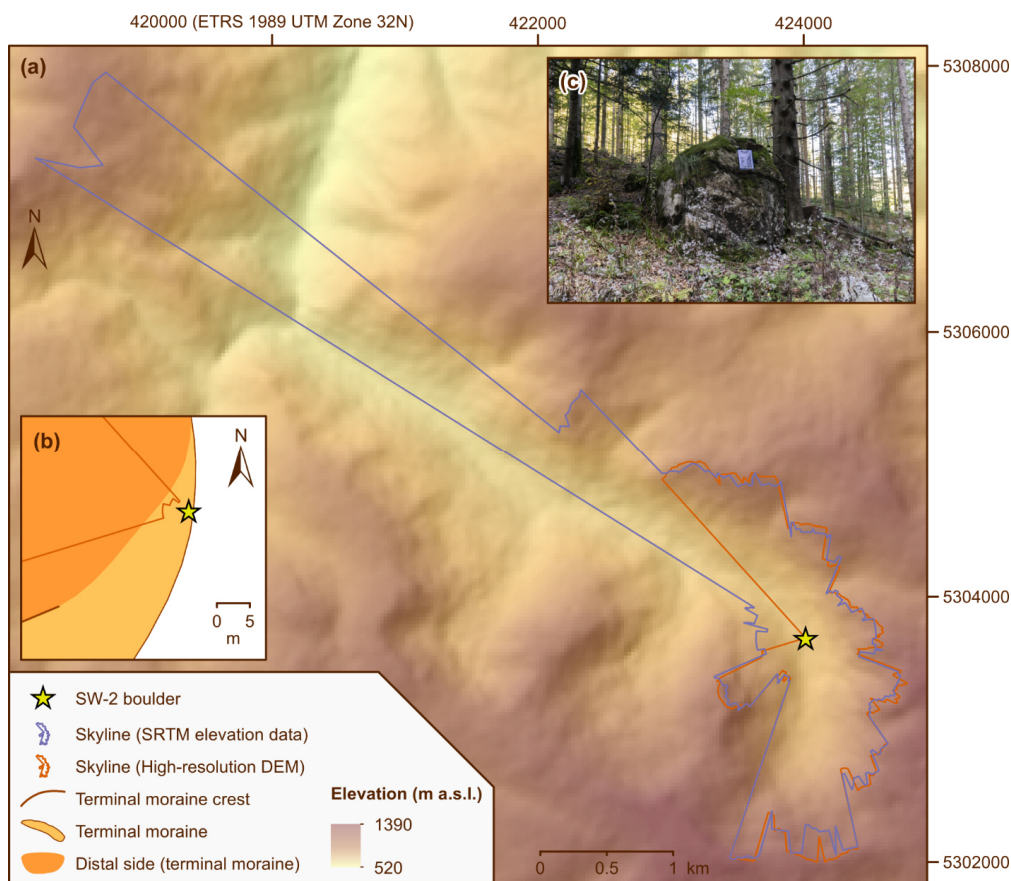
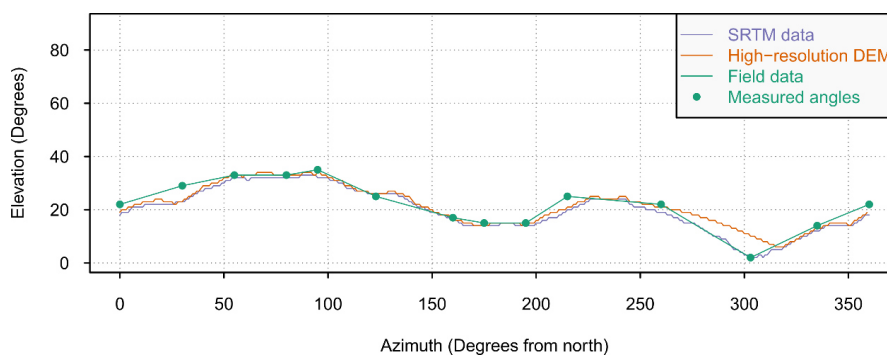


Figure 12: (a) Map of the area around the SW-2 boulder and skylines generated with the skyline function in ArcMap 10.8.1. The shaded relief in the background was derived from SRTM elevation data (NASA Jet Propulsion Laboratory, 2013). (b) Detailed map of the area around the SW-2 boulder. The skyline generated with the high-resolution DEM shows that the intensity of cosmic radiation at the sampling surface on the SW-2 boulder is apparently reduced by the moraine crest. (c) Photo of the SW-2 boulder and of the proximal side of the moraine.



The TanDEM-X data-based shielding factors for the FS-1a, FS-2a, SW-2, SW-9 and WH-1a boulders did not agree with field-
410 data based shielding factors (Fig. 5d). Except of the SW-9 boulder, these boulders were situated in areas covered by mixed
and coniferous forests. As TanDEM-X data are not corrected for vegetation, differing canopy heights and small-sized
anomalies in vegetation cover were probably misinterpreted as topographical obstructions by the toolbox. The SW-9 boulder,
for example, was situated in open grassland close to a coniferous forest. Measuring pairs of azimuth and elevation angles in
the field turned out to be straightforward during fieldwork. The horizon around the boulder was even visible through the
415 coniferous forest. Inspecting the skyline for the SW-9 boulder in ArcMap 10.8.1 revealed that the edge of the coniferous forest
was misinterpreted as topographical barrier by the toolbox. Excluding the shielding factors for the FS-1a, FS-2a, SW-2, SW-
9 and WH-1a boulders led to a strong correlation with field-data based shielding factors (Fig. 11d). Therefore, TanDEM-X
data should only be used if there is little vegetation in the surroundings of sampling sites.



420

Figure 13: Horizon around the sampling surface on the SW-2 boulder according to SRTM data, the high-resolution DEM and field data. Elevation and azimuth angles were computed with the skyline and skytable functions in ArcMap 10.8.1.

Although shielding factors determined with the high-resolution DEM were generally very consistent with field-data based
425 shielding factors, the shielding factors for the FS-1a, FS-2a and SW-9 boulders did not agree (Fig. 5f). As outlined above, the
mismatch between the shielding factors is, most likely, due to the low reliability of field data. The inspection of the skyline
around the SW-2 boulder revealed an additional explanation for the discrepancy. According to the skyline, the nearby moraine



crest apparently induced topographic shielding (Fig. 12). Field observations clearly contradict this assumption (Fig. 13). This suggests that small-sized topographical obstructions in the vicinity of sampling sites may lead to incorrect shielding factors if elevation data with a very high xy -resolution are used and if only imprecise coordinates of sampling sites are available. Excluding the potentially “problematic” shielding factors for the FS-1a, FS-2a and SW-9 boulders led to a considerably better agreement between the shielding factors ($R^2 = 0.99$; $p < 0.05$; Fig. 11f).

5.2 Impact of the spatial resolution of elevation data on shielding factors

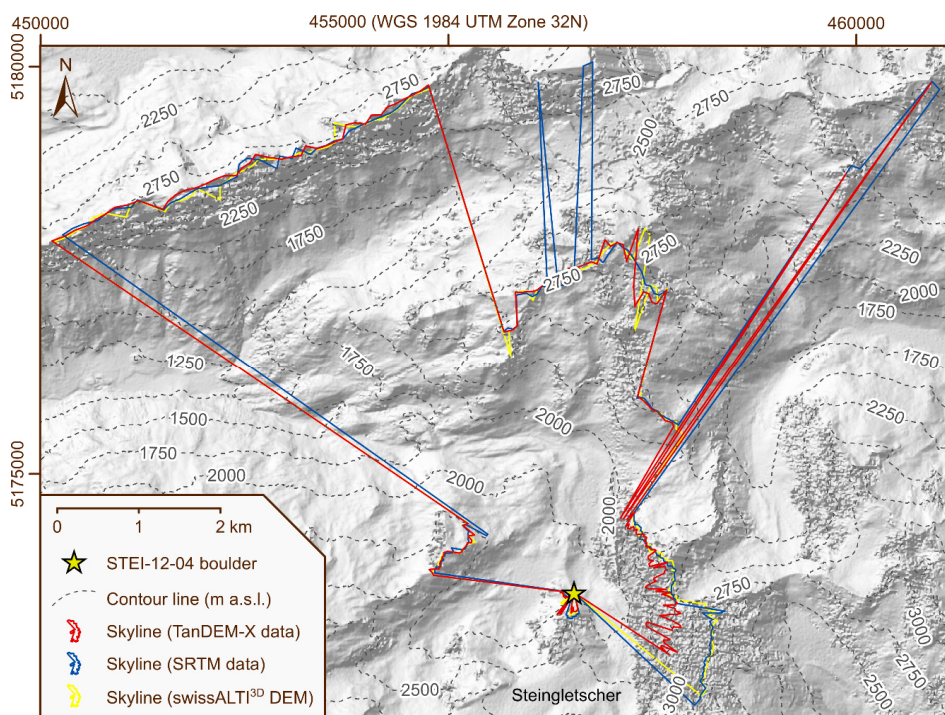
The high-resolution, vegetation-corrected DEM and two resampled versions yielded very similar shielding factors for boulders in the southern Black Forest. Similarly, the fit between GIS-based and field data-based shielding factors for boulders in the forefield of Steingletscher was independent of the xy -resolution of the resampled versions of the swissALTI^{3D} DEM. TanDEM-X data-based shielding factors for boulders in the forefield of Steingletscher were, however, most consistent with field data-based shielding factors (Fig. 9c & d). The inspection of skylines for moraine boulders contradicts the view that these shielding factors were most robust. As the topography should be more accurately represented in the swissALTI^{3D} DEM due to the higher spatial resolution, the skylines derived from TanDEM-X data were compared with the swissALTI^{3D} DEM. This comparison revealed that skylines derived from TanDEM-X data did not match the topography represented in the swissALTI^{3D} DEM. Discrepancies were observed on steep slopes. These are not well represented in TanDEM-X elevation data and, hence, TanDEM-X data of the region around Steingletscher is quite noisy (Fig. 14). The skylines for the STEI-12-04 boulder derived from the swissALTI^{3D} DEM and SRTM data were, for example, consistent (Fig. 14). Due to noise, the TanDEM-X data-based skyline for the STEI-12-04 boulder should not be considered realistic (Fig. 14). If one wants to use TanDEM-X data for shielding factor calculations, the data of the region of interest should be carefully checked before shielding factor calculations and, in case of doubt, skylines should be inspected. The hypothesis that the robustness of the shielding factors is independent of the xy -resolution of the input-DEM is further supported by the observation that SRTM data and the swissALTI^{3D} DEM performed equally well.

450

These observations lead to the conclusion that high-resolution elevation data are not necessary for shielding factor calculations. The use of elevation data with a lower spatial resolution has two advantages: Running the toolbox with elevation data with a



lower spatial resolution takes less computational time. In addition, there is a lower risk that small-scale topographical irregularities in the vicinity of the sampling sites of boulders (Fig. 12a) lead to errors during shielding factor calculations. Due
455 to the larger pixel size of the elevation data, precise coordinates of sampling sites should be less crucial. very precise xy -coordinates are a prerequisite for the use of elevation data with a very high spatial resolution.



460 **Figure 14: Skylines for the STEI-12-04 boulder in the forefield of Steingletscher derived from TanDEM-X data, SRTM data and the swissALTI^{3D} DEM. The hillshade image in the background was derived from TanDEM-X data (©DLR 2021), whereas the contour lines are based on a resampled version of the swissALTI^{3D} DEM (xy -resolution: 1m).**



465 Norton and Vanacker (2009) demonstrated that small topographical obstructions do not necessarily induce shielding from
cosmic rays. If the distance that cosmic rays penetrate through the topographical anomaly is not significantly higher or even
lower than the particle attenuation length, a portion of cosmic rays will travel through the object without any interaction.
Supposing that this interaction becomes measurable only if this distance is equivalent or larger than the particle attenuation
length, measurable topographic shielding only occurs if the largest distance that cosmic rays penetrate through an obstruction
is equivalent to the particle attenuation length (Norton and Vanacker, 2009). Assuming an attenuation length of 160 g cm^{-2} ,
470 the depth at which 63% of the cosmic rays have been stopped will be 61.5 cm for granite (assumed density: $\sim 2.6 \text{ g cm}^{-3}$; Gosse
and Phillips, 2001). Norton and Vanacker (2009) recommend avoiding a potential effect on topographic shielding factors by
selecting DEMs with larger pixel sizes. As a rule of thumb, they propose the use of DEMs with a pixel size of 5 m. Quantifying
the effect of small-sized topographic anomalies on topographic shielding factors is not possible here. This would require the
development of a new GIS-based tool that takes the dimensions of topographical obstructions into account.

475 **5.3 Influence of the type of the elevation model on shielding factors**

The fit between the GIS-based shielding factors and those from field data for boulders in the southern Black Forest turned out
to be highest when vegetation-corrected elevation data was selected as input-data for the toolbox. This finding is not surprising,
as both SRTM and TanDEM-X elevation data were not corrected for vegetation. This leads to the conclusion that the type of
the elevation model, i.e. corrected for vegetation or not, determines the quality of shielding factors for sites in forested areas.
480 Whenever available, vegetation-corrected elevation data should be chosen for the site of interest. The use of TanDEM-X data
led to a weaker correlation between the GIS- and the field data-based topographic shielding factors. As discussed in Sect. 5.1,
small-sized anomalies in vegetation cover that are represented in TanDEM-X data explain the lower fit between the shielding
factors. Therefore, if sampling sites are situated in forested areas and a vegetation-corrected DEM is not available for the area
of interest, a DSM with a rather low spatial resolution, such as SRTM data, is the best option.



485 **5.4 Correcting for the boulder height – does it matter?**

Incorporating the boulder height during the computation of topographic shielding factors led to a similar correlation between the shielding factors (Figs. 4f & 9) or further increased the fit (Figs. 4b, 4d, 5b & 7b). Considering the height of the boulders during shielding factor calculations only led in one case to a slightly lower fit between the shielding factors (Fig. Figure 8b). Correcting shielding factors for the boulder height is therefore recommended.

490 **5.5 Implications of the sensitivity experiments**

Recalculating CRE ages of moraine boulders in the southern Black Forest led, in most cases, to minor changes in CRE ages (<1%). As these shifts in CRE ages would not have an effect on the interpretation proposed by Hofmann et al. (2022), SRTM data seem to be sufficient to compute shielding factors for sampling sites in flat or low mountainous areas. If boulders on landforms of a known age are targeted for establishing production rate reference sites, the use of elevation data with a comparably low spatial resolution could introduce additional errors. The use of SRTM data-based shielding factors instead of field data-based shielding factors resulted in a more pronounced change in CRE ages of boulders in the Écrins massif. The average CRE age difference amounted to 1.6% with respect to the ages calculated with the field-data based shielding factors. As can be seen in Table 3, the CRE age difference was highest for the boulders with the youngest CRE ages and amounted up to 4.1%. The comparably large shift of CRE ages is probably due to the relatively weak correlation between the GIS-based and field data-based shielding factors ($R^2 = 0.74$). It remains unclear whether this relatively low fit is due to a low quality of field data or imprecise GIS-based shielding factors. As most of the recalculated CRE ages of boulders on moraines of Steingletscher remained unchanged when GIS-based topographic shielding factors were chosen for CRE age calculations, the choice of the shielding factors does not seem to have a substantial influence on CRE ages if recently exposed surfaces in high Alpine settings are targeted for CRE dating.

505 **6 Conclusion**

In an earlier validation study, Li (2018) noted that his point-based toolbox provides stable shielding factors for DEMs with different spatial resolutions. Tests with high-resolution DEMs and resampled versions with a lower xy -resolution confirm this view. This rule applies to the studied low mountainous area and the high Alpine settings. It is shown that precise xy -coordinates



of sampling sites must be imperatively used if one wants to use elevation data with a very high spatial resolution. If coordinates
510 are imprecise there is a risk that small-scale objects in the surroundings of sampling sites are interpreted as topographical
obstructions by the toolbox even though they do not induce topographic shielding. Therefore, elevation data with a lower
spatial resolution should be preferably used to save computational time and to avoid unnecessary problems associated with
small-scale topographical irregularities in the vicinity of sampling sites. Unsurprisingly, the use of vegetation-corrected
elevation data allowed for calculating shielding factors that match better field data-based shielding factors. If vegetation-
515 corrected elevation data is not available for a site, a DSM with a low spatial resolution should be chosen since small-scale
irregularities in the vegetation cover are not represented in these data. Replacing field data-based shielding factors by SRTM
data-based shielding factors during CRE age calculations led, in most cases, to minor shifts in CRE ages and only in few cases
to changes in the order of a few per cent. Incorporating the height above ground of the sampling surfaces led to a similar
agreement between the shielding factors or further increased the fit and, hence, shielding factors should be corrected for the
520 boulder height. Overall, the toolbox of Li (2018) provides a promising approach for calculating topographic shielding factors
if suitable elevation data is chosen. Due to the high robustness of the results, the toolbox should therefore be used more widely
in the field of geochronology.

Data availability

The data supporting this study are available from the author upon reasonable request.

525 **Competing interests**

The author declares that he has no conflict of interest.

Acknowledgements

F.M. Hofmann is a recipient of a PhD fellowship of *Studienstiftung des Deutschen Volkes*. This research was also financially
supported by the German Research Foundation through the ‘Geometry, chronology and dynamics of the last Pleistocene
530 glaciation of the Black Forest’ project (grant no. 426333515) granted to Frank Preusser. Melaine Le Roy and Irene



Schimmelpfennig are acknowledged for providing additional data for CRE age recalculations. Florian Rauscher is thanked for his help during fieldwork. The author thanks the local farmers and landowners for permission to collect field data on their properties. The author expresses his gratitude to the nature protection and the forest protection, biodiversity and silviculture departments of the Freiburg regional council as well as to the administration of the Feldberg natural reserve, particularly
535 Clemens Glunk, Albrecht Franke and Achim Laber, for the permission to access the sampling sites. The forestry department of the Breisgau-Hochschwarzwald county provided a forest access permit. Stefan Hergarten and Martin Margold are thanked for insightful discussions on earlier versions of the manuscript.

References

- Balco, G.: Topographic shielding calculator, http://stoneage.ice-d.org/math/skyline/skyline_in.html, last access: 23 February
540 2021, 2018.
- Balco, G., Stone, J. O., Lifton, N. A., and Dunai, T. J.: A complete and easily accessible means of calculating surface exposure ages or erosion rates from ^{10}Be and ^{26}Al measurements, *Quat. Geochronol.*, 3, 174–195, <https://doi.org/10.1016/j.quageo.2007.12.001>, 2008.
- Baroni, C., Gennaro, S., Salvatore, M. C., Ivy-Ochs, S., Christl, M., Cerrato, R., and Orombelli, G.: Last Lateglacial glacier
545 advance in the Gran Paradiso Group reveals relatively drier climatic conditions established in the Western Alps since at least the Younger Dryas, *Quaternary Sci. Rev.*, 255, 106815, <https://doi.org/10.1016/j.quascirev.2021.106815>, 2021.
- Barr, I. D. and Lovell, H.: A review of topographic controls on moraine distribution, *Geomorphology*, 226, 44–64, <https://doi.org/10.1016/j.geomorph.2014.07.030>, 2014.
- Boxleitner, M., Ivy-Ochs, S., Egli, M., Brandova, D., Christl, M., Dahms, D., and Maisch, M.: The ^{10}Be deglaciation
550 chronology of the Göschenental, central Swiss Alps, and new insights into the Göschenen Cold Phases, *Boreas*, 48, 867–878, <https://doi.org/10.1111/bor.12394>, 2019.
- Braumann, S. M., Schaefer, J. M., Neuhuber, S. M., Reitner, J. M., Lühgens, C., and Fiebig, M.: Holocene glacier change in the Silvretta Massif (Austrian Alps) constrained by a new ^{10}Be chronology, historical records and modern observations, *Quaternary Sci. Rev.*, 245, 106493, <https://doi.org/10.1016/j.quascirev.2020.106493>, 2020.



- 555 Briner, J. P.: Dating Glacial Landforms, in: Encyclopedia of snow, ice and glaciers, edited by: Singh, V. P., Springer, Dordrecht, 175–186, https://doi.org/10.1007/978-90-481-2642-2_616, 2011.
- Brown, E. T., Edmond, J. M., Raisbeck, G. M., Yiou, F., Kurz, M. D., and Brook, E. J.: Examination of surface exposure ages of Antarctic moraines using in situ produced ^{10}Be and ^{26}Al , *Geochim. Cosmochim. Ac.*, 55, 2269–2283, [https://doi.org/10.1016/0016-7037\(91\)90103-C](https://doi.org/10.1016/0016-7037(91)90103-C), 1991.
- 560 Cardinal, T., Audin, L., Rolland, Y., Schwartz, S., Petit, C., Zerathe, S., Borgniet, L., Braucher, R., Nomade, J., Dumont, T., and Guillou, V.: Interplay of fluvial incision and rockfalls in shaping periglacial mountain gorges, *Geomorphology*, 381, 107665, <https://doi.org/10.1016/j.geomorph.2021.107665>, 2021.
- Claude, A., Ivy-Ochs, S., Kober, F., Antognini, M., Salcher, B., and Kubik, P. W.: The Chironico landslide (Valle Leventina, southern Swiss Alps): age and evolution, *Swiss J. Geosci.*, 107, 273–291, <https://doi.org/10.1007/s00015-014-0170-z>,
565 2014.
- Codilean, A. T.: Calculation of the cosmogenic nuclide production topographic shielding scaling factor for large areas using DEMs, *Earth Surf. Proc. Land.*, 31, 785–794, <https://doi.org/10.1002/esp.1336>, 2006.
- DLR: TanDEM-X - Digital Elevation Model (DEM) - Global, 12m, 2016.
- Dong, G., Zhou, W., Fu, Y., Zhang, L., Zhao, G., and Li, M.: The last glaciation in the headwater area of the Xiaokelanhe
570 River, Chinese Altai: Evidence from ^{10}Be exposure-ages, *Quat. Geochronol.*, 56, 101054, <https://doi.org/10.1016/j.quageo.2020.101054>, 2020.
- Dormann, C.: Hypotheses and Tests, in: *Environmental Data Analysis: An Introduction with Examples in R*, Springer International Publishing, Cham, 177–184, https://doi.org/10.1007/978-3-030-55020-2_13, 2020.
- Dunai, T. J. and Stuart, F. M.: Reporting of cosmogenic nuclide data for exposure age and erosion rate determinations, *Quat. Geochronol.*, 4, 437–440, <https://doi.org/10.1016/j.quageo.2009.04.003>, 2009.
575
- Dunne, J., Elmore, D., and Muzikar, P.: Scaling factors for the rates of production of cosmogenic nuclides for geometric shielding and attenuation at depth on sloped surfaces, *Geomorphology*, 27, 3–11, [https://doi.org/10.1016/S0169-555X\(98\)00086-5](https://doi.org/10.1016/S0169-555X(98)00086-5), 1999.



- Farr, T. G., Rosen, P. A., Caro, E., Crippen, R., Duren, R., Hensley, S., Kobrick, M., Paller, M., Rodriguez, E., Roth, L., Seal, D., Shaffer, S., Shimada, J., Umland, J., Werner, M., Oskin, M., Burbank, D., and Alsdorf, D.: The Shuttle Radar Topography Mission, *Rev. Geophys.*, 45, <https://doi.org/10.1029/2005RG000183>, 2007.
- Fernandes, M., Oliva, M., Vieira, G., Palacios, D., Fernández-Fernández, J. M., Garcia-oteyza, J., Schimmelpfennig, I., ASTER Team, and Antoniades, D.: Glacial oscillations during the Bølling–Allerød Interstadial–Younger Dryas transition in the Ruda Valley, Central Pyrenees, *J. Quaternary Sci.*, 37, 42–58, <https://doi.org/10.1002/jqs.3379>, 2022.
- 585 Fernandes, M., Oliva, M., Vieira, G., Palacios, D., Fernández-Fernández, J. M., Delmas, M., García-Oteyza, J., Schimmelpfennig, I., Ventura, J., Aumaitre, G., and Keddadouche, K.: Maximum glacier extent of the Penultimate Glacial Cycle in the Upper Garonne Basin (Pyrenees): new chronological evidence, *Environ. Earth Sci.*, 80, <https://doi.org/10.1007/s12665-021-10022-z>, 2021.
- Fernández-Fernández, J. M., Palacios, D., Andrés, N., Schimmelpfennig, I., Tanarro, L. M., Brynjólfsson, S., López-Acevedo, F. J., Sæmundsson, Þ., and ASTER Team: Constraints on the timing of debris-covered and rock glaciers: An exploratory case study in the Hólar area, northern Iceland, *Geomorphology*, 361, 107196, <https://doi.org/10.1016/j.geomorph.2020.107196>, 2020.
- Gosse, J. C. and Phillips, F. M.: Terrestrial in situ cosmogenic nuclides: theory and application, *Quaternary Sci. Rev.*, 20, 1475–1560, [https://doi.org/10.1016/S0277-3791\(00\)00171-2](https://doi.org/10.1016/S0277-3791(00)00171-2), 2001.
- 595 Hofmann, F. M., Preusser, F., Schimmelpfennig, I., Léanni, L., and ASTER Team: Late Pleistocene glaciation history of the southern Black Forest, Germany: ^{10}Be cosmic-ray exposure dating and equilibrium line altitude reconstructions in Sankt Wilhelmer Tal, *J. Quaternary Sci.*, 37, 688–706, <https://doi.org/10.1002/jqs.3407>, 2022.
- Hofmann, F. M., Alexanderson, H., Schoeneich, P., Mertes, J. R., Léanni, L., and ASTER Team: Post-Last Glacial Maximum glacier fluctuations in the southern Écrins massif (westernmost Alps): insights from ^{10}Be cosmic ray exposure dating, *Boreas*, 48, 1019–1041, <https://doi.org/10.1111/bor.12405>, 2019.
- 600 Ivy-Ochs, S. and Kober, F.: Surface exposure dating with cosmogenic nuclides, *E&G Quaternary Sci. J.*, 57, 179–209, <https://doi.org/10.3285/eg.57.1-2.7>, 2008.



- Ivy-Ochs, S., Kerschner, H., Reuther, A., Preusser, F., Heine, K., Maisch, M., Kubik, P. W., and Schlüchter, C.: Chronology of the last glacial cycle in the European Alps, *J. Quaternary Sci.*, 23, 559–573, <https://doi.org/10.1002/jqs.1202>, 2008.
- 605 Krieger, G., Moreira, A., Fiedler, H., Hajnsek, I., Werner, M., Younis, M., and Zink, M.: TanDEM-X: A satellite formation for high-resolution SAR interferometry, *IEEE T. Geosci. Remote*, 45, 3317–3341, <https://doi.org/10.1109/TGRS.2007.900693>, 2007.
- Lal, D.: Cosmic ray labeling of erosion surfaces: in situ nuclide production rates and erosion models, *Earth and Planet. Sc. Lett.*, 104, 424–439, [https://doi.org/10.1016/0012-821X\(91\)90220-C](https://doi.org/10.1016/0012-821X(91)90220-C), 1991.
- 610 Le Roy, M., Deline, P., Carcaillet, J., Schimmelpfennig, I., Ermini, M., and ASTER Team: ^{10}Be exposure dating of the timing of Neoglacial glacier advances in the Ecrins-Pelvoux massif, southern French Alps, *Quaternary Sci. Rev.*, 178, 118–138, <https://doi.org/10.1016/j.quascirev.2017.10.010>, 2017.
- Li, Y.-K.: Determining topographic shielding from digital elevation models for cosmogenic nuclide analysis: a GIS model for discrete sample sites, *J. Mt. Sci.*, 15, 939–947, <https://doi.org/10.1007/s11629-018-4895-4>, 2018.
- 615 Li, Y.-K.: Determining topographic shielding from digital elevation models for cosmogenic nuclide analysis: a GIS approach and field validation, *J. Mt. Sci.*, 10, 355–362, <https://doi.org/10.1007/s11629-013-2564-1>, 2013.
- Mackintosh, A. N., Anderson, B. M., and Pierrehumbert, R. T.: Reconstructing Climate from Glaciers, *Annu. Rev. Earth Pl. Sc.*, 45, 649–680, <https://doi.org/10.1146/annurev-earth-063016-020643>, 2017.
- Martin, L. C. P., Blard, P. H., Balco, G., Lavé, J., Delunel, R., Lifton, N., and Laurent, V.: The CREp program and the ICE-D production rate calibration database: A fully parameterizable and updated online tool to compute cosmic-ray exposure ages, *Quat. Geochronol.*, 38, 25–49, <https://doi.org/10.1016/j.quageo.2016.11.006>, 2017.
- 620 Mohren, J., Binnie, S. A., Ritter, B., and Dunai, T. J.: Development of a steep erosional gradient over a short distance in the hyperarid core of the Atacama Desert, northern Chile, *Global Planet. Change*, 184, 103068, <https://doi.org/10.1016/j.gloplacha.2019.103068>, 2020.
- 625 Muscheler, R., Beer, J., Kubik, P. W., and Synal, H. A.: Geomagnetic field intensity during the last 60,000 years based on ^{10}Be and ^{36}Cl from the Summit ice cores and ^{14}C , *Quaternary Sci. Rev.*, 24, 1849–1860, <https://doi.org/10.1016/j.quascirev.2005.01.012>, 2005.



- NASA Jet Propulsion Laboratory: NASA Shuttle Radar Topography Mission Global 1 arc second, <https://doi.org/10.5067/MEaSURES/SRTM/SRTMGL1.003>, 2013.
- 630 Nishiizumi, K., Winterer, E. L., Kohl, C. P., Klein, J., Middleton, R., Lal, D., and Arnold, J. R.: Cosmic ray production rates of ^{10}Be and ^{26}Al in quartz from glacially polished rocks, *J. Geophys. Res.-Sol. Ea.*, 94, 17907–17915, <https://doi.org/10.1029/JB094iB12p17907>, 1989.
- Norton, K. P. and Vanacker, V.: Effects of terrain smoothing on topographic shielding correction factors for cosmogenic nuclide-derived estimates of basin-averaged denudation rates, *Earth Surf. Proc. Land.*, 34, 145–154, 635 <https://doi.org/10.1002/esp.1700>, 2009.
- Oliva, M., Fernandes, M., Palacios, D., Fernández-Fernández, J.-M., Schimmelpfennig, I., Antoniadis, D., Aumaitre, G., Bourlès, D., and Keddadouche, K.: Rapid deglaciation during the Bølling-Allerød Interstadial in the Central Pyrenees and associated glacial and periglacial landforms, *Geomorphology*, 385, 107735, <https://doi.org/10.1016/j.geomorph.2021.107735>, 2021.
- 640 Oliva, M., Palacios, D., Fernández-Fernández, J. M., Rodríguez-Rodríguez, L., García-Ruiz, J. M., Andrés, N., Carrasco, R. M., Pedraza, J., Pérez-Alberti, A., Valcárcel, M., and Hughes, P. D.: Late Quaternary glacial phases in the Iberian Peninsula, *Earth-Sci. Rev.*, 192, 564–600, <https://doi.org/10.1016/j.earscirev.2019.03.015>, 2019.
- Palacios, D., Rodríguez-Mena, M., Fernández-Fernández, J. M., Schimmelpfennig, I., Tanarro, L. M., Zamorano, J. J., Andrés, N., Úbeda, J., Sæmundsson, Þ., Brynjólfsson, S., Oliva, M., and ASTER Team: Reversible glacial-periglacial transition 645 in response to climate changes and paraglacial dynamics: A case study from Hédinsdalsjökull (northern Iceland), *Geomorphology*, 388, 107787, <https://doi.org/10.1016/j.geomorph.2021.107787>, 2021.
- Peng, X., Chen, Y., Li, Y., Liu, B., Liu, Q., Yang, W., Cui, Z., and Liu, G.: Late Holocene glacier fluctuations in the Bhutanese Himalaya, *Global Planet. Change*, 187, 103137, <https://doi.org/10.1016/j.gloplacha.2020.103137>, 2020.
- Phillips, F. M., Argento, D. C., Balco, G., Caffee, M. W., Clem, J., Dunai, T. J., Finkel, R., Goehring, B., Gosse, J. C., Hudson, 650 A. M., Jull, A. T., Kelly, M. A., Kurz, M., Lal, D., Lifton, N., Marrero, S. M., Nishiizumi, K., Reedy, R. C., Schaefer, J., Stone, J. O., Swanson, T., and Zreda, M. G.: The CRONUS-Earth Project: A synthesis, *Quat. Geochronol.*, 31, 119–154, <https://doi.org/10.1016/j.quageo.2015.09.006>, 2016.



- R Core Team: R: A language and environment for statistical computing, R Foundation for Statistical Computing, Vienna, 2021.
- 655 Rabus, B., Eineder, M., Roth, A., and Bamler, R.: The shuttle radar topography mission—a new class of digital elevation models acquired by spaceborne radar, *ISPRS J. Photogramm.*, 57, 241–262, [https://doi.org/10.1016/S0924-2716\(02\)00124-7](https://doi.org/10.1016/S0924-2716(02)00124-7), 2003.
- Rizzoli, P., Martone, M., Gonzalez, C., Wecklich, C., Borla Tridon, D., Bräutigam, B., Bachmann, M., Schulze, D., Fritz, T., Huber, M., Wessel, B., Krieger, G., Zink, M., and Moreira, A.: Generation and performance assessment of the global
660 TanDEM-X digital elevation model, *ISPRS J. Photogramm.*, 132, 119–139, <https://doi.org/10.1016/j.isprsjprs.2017.08.008>, 2017.
- Rodríguez, E., Morris, C. S., and Belz, J. E.: A Global Assessment of the SRTM Performance, *Photogramm. Eng. Rem. S.*, 72, 249–260, <https://doi.org/10.14358/PERS.72.3.249>, 2006.
- RStudio Team: RStudio: Integrated Development Environment for R, RStudio, PBC, Boston, 2021.
- 665 Rudolph, E. M., Hedding, D. W., Fabel, D., Hodgson, D. A., Gheorghiu, D. M., Shanks, R., and Nel, W.: Early glacial maximum and deglaciation at sub-Antarctic Marion Island from cosmogenic ^{36}Cl exposure dating, *Quaternary Sci. Rev.*, 231, 106208, <https://doi.org/10.1016/j.quascirev.2020.106208>, 2020.
- Santos-González, J., González-Gutiérrez, R. B., Redondo-Vega, J. M., Gómez-Villar, A., Jomelli, V., Fernández-Fernández, J. M., Andrés, N., García-Ruiz, J. M., Peña-Pérez, S. A., Melón-Nava, A., Oliva, M., Álvarez-Martínez, J., Charton, J.,
670 and Palacios, D.: The origin and collapse of rock glaciers during the Bølling-Allerød interstadial: A new study case from the Cantabrian Mountains (Spain), *Geomorphology*, 401, 108112, <https://doi.org/10.1016/j.geomorph.2022.108112>, 2022.
- Schaefer, J. M., Denton, G. H., Kaplan, M., Putnam, A., Finkel, R. C., Barrell, D. J. A., Andersen, B. G., Schwartz, R., Mackintosh, A., Chinn, T., and Schlüchter, C.: High-Frequency Holocene Glacier Fluctuations in New Zealand Differ from the Northern Signature, *Science*, 324, 622–625, <https://doi.org/10.1126/science.1169312>, 2009.
- 675 Schimmelpfennig, I., Schaefer, J. M., Akçar, N., Koffman, T., Ivy-Ochs, S., Schwartz, R., Finkel, R. C., Zimmerman, S., and Schlüchter, C.: A chronology of Holocene and Little Ice Age glacier culminations of the Steingletscher, Central Alps,



- Switzerland, based on high-sensitivity beryllium-10 moraine dating, *Earth Planet. Sc. Lett.*, 393, 220–230,
<https://doi.org/10.1016/j.epsl.2014.02.046>, 2014.
- Sharp, M.: Surging glaciers, *Progress in Physical Geography: Earth and Environment*, 12, 533–559,
680 <https://doi.org/10.1177/030913338801200403>, 1988.
- Shean, D.: High Mountain Asia 8-meter DEM Mosaics Derived from Optical Imagery, Version 1,
<https://doi.org/10.5067/KXOVQ9L172S2>, 2017.
- Siame, L. L., Braucher, R., and Bourlès, D.: Les nucléides cosmogéniques produits *in-situ* des nouveaux outils en
géomorphologie quantitative, *Bull. Soc. Geo. Fr.*, 171, 383–396, <https://doi.org/10.2113/171.4.383>, 2000.
- 685 Stone, J. O.: Air pressure and cosmogenic isotope production, *J. Geophys. Res.-Sol. Ea.*, 105, 23753–23759,
<https://doi.org/10.1029/2000JB900181>, 2000.
- Tanarro, L. M., Palacios, D., Fernández-Fernández, J. M., Andrés, N., Oliva, M., Rodríguez-Mena, M., Schimmelpfennig, I.,
Brynjólfsson, S., Sæmundsson, Þ., Zamorano, J. J., Úbeda, J., Aumaître, G., Bourlès, D., and Keddadouche, K.: Origins
of the divergent evolution of mountain glaciers during deglaciation: Hofsdalur cirques, Northern Iceland, *Quaternary Sci.*
690 *Rev.*, 273, 107248, <https://doi.org/10.1016/j.quascirev.2021.107248>, 2021.
- Uppala, S. M., Kållberg, P. W., Simmons, A. J., Andrae, U., Da Bechtold, V. C., Fiorino, M., Gibson, J. K., Haseler, J.,
Hernandez, A., Kelly, G. A., Li, X., Onogi, K., Saarinen, S., Sokka, N., Allan, R. P., Andersson, E., Arpe, K., Balmaseda,
M. A., Beljaars, A. C. M., van Berg, L. de, Bidlot, J., Bormann, N., Caires, S., Chevallier, F., Dethof, A., Dragosavac, M.,
Fisher, M., Fuentes, M., Hagemann, S., Hólm, E., Hoskins, B. J., Isaksen, I., Janssen, P. A. E. M., Jenne, R., McNally,
695 A. P., Mahfouf, J. F., Morcrette, J. J., Rayner, N. A., Saunders, R. W., Simon, P., Sterl, A., Trenberth, K. E., Untch, A.,
Vasiljevic, D., Viterbo, P., and Woollen, J.: The ERA-40 re-analysis, *Q. J. Roy. Meteor. Soc.*, 131, 2961–3012,
<https://doi.org/10.1256/qj.04.176>, 2005.
- Valentino, J. D., Owen, L. A., Spotila, J. A., Cesta, J. M., and Caffee, M. W.: Timing and extent of Late Pleistocene glaciation
in the Chugach Mountains, Alaska, *Quat. Res.*, 101, 205–224, <https://doi.org/10.1017/qua.2020.106>, 2021.
- 700 Vermeesch, P.: CosmoCalc: An Excel add-in for cosmogenic nuclide calculations, *Geochem. Geophys. Geosy.*, 8,
<https://doi.org/10.1029/2006GC001530>, 2007.